

# Nonlinear droop compensation for current waveforms in MRI gradient systems

Reza Babaloo<sup>1,2</sup>  | Ergin Atalar<sup>1,2</sup> 

<sup>1</sup>National Magnetic Resonance Research Center (UMRAM), Bilkent University, Ankara, Turkey

<sup>2</sup>Department of Electrical and Electronics Engineering, Bilkent University, Ankara, Turkey

## Correspondence

Ergin Atalar, National Magnetic Resonance, Research Center (UMRAM) & Department of Electrical and Electronics Engineering, Bilkent University, 06800 Bilkent, Ankara, Turkey.  
Email: [ergin.atalar@bilkent.edu.tr](mailto:ergin.atalar@bilkent.edu.tr)

**Purpose:** Providing accurate gradient currents is challenging due to the gradient chain nonlinearities, arising from gradient power amplifiers and power supply stages. This work introduces a new characterization approach that takes the amplifier and power supply into account, resulting in a nonlinear model that compensates for the current droop.

**Methods:** The gradient power amplifier and power supply stage were characterized by a modified state-space averaging technique. The resulting nonlinear model was inverted and used in feedforward to control the gradient coil current. A custom-built two-channel  $z$ -gradient coil was driven by high-switching (1 MHz), low-cost amplifiers (<\$200) using linear and nonlinear controllers. High-resolution (<80 ps) pulse-width-modulation signals were used to drive the amplifiers. MRI experiments were performed to validate the nonlinear controller's effectiveness.

**Results:** The simulation results validated the functionality of the state-space averaging method in characterizing the gradient system. The performance of linear and nonlinear controllers in generating a trapezoidal current waveform was compared in simulations and experiments. The integral errors between the desired waveform and waveforms generated by linear and nonlinear controllers were 1.9% and 0.13%, respectively, confirming the capability of the nonlinear controller to compensate for the current droop. Phantom images validated the nonlinear controller's ability to correct droop-induced distortions.

**Conclusion:** Benchtop measurements and MRI experiments demonstrated that the proposed nonlinear characterization and digitally implemented feedforward controller could drive gradient coils with droop-free current waveforms (without a feedback loop). In experiments, the nonlinear controller outperformed the linear controller by a 14-fold reduction in the integral error of a test waveform.

## KEYWORDS

droop compensation, gradient array, high-switching gradient power amplifier, MRI gradient system characterization, nonlinear feedforward controller, state-space averaging

## 1 | INTRODUCTION

MRI scanners use three gradient coils to provide spatial encoding within an imaging volume. Gradient power amplifiers (GPAs) with high-voltage and high-current specifications drive the gradient coils. The current flowing through each coil must follow a command waveform as accurately as possible to ensure good image quality. However, providing accurate gradient coil currents might be challenging due to hardware imperfections. Conventional gradient systems use closed-loop feedback controllers<sup>1,2</sup> to precisely track the command input current. Thus, they require high-precision high-cost current sensors because any error in the current measurements results in an output error. The recently introduced gradient array systems,<sup>3–5</sup> multi-coil technique,<sup>6–8</sup> and matrix gradient coils,<sup>9,10</sup> which are capable of generating dynamically controllable magnetic field profiles, use multiple gradient coils and, hence, need many current sensors for the feedback loop, which significantly increases the system cost (>\$600 per sensor). Therefore, to avoid the need for measurement data and expensive current sensors, feedforward controllers might be preferable.

In an ideal system, the gradient amplifiers are powered by a constant voltage at all times. However, in a practical system, the power supply gradually loses its voltage when it starts to deliver a high current. The gradual decrease in the supply voltage is called droop<sup>11–13</sup> and causes a gradual decrease in the current at the flat top of a gradient pulse if there is no feedback. To use feedforward controllers effectively, an approximate system model should be available. Ertan et al.<sup>3</sup> considered a linear time-invariant first-order model of the gradient system in the feedforward, including only the gradient coil model. The GPAs were assumed to generate an ideal voltage source while ignoring the potential droop in the supply. However, as discussed in this work, the droop is a nonlinear process that cannot be corrected with a linear time-invariant controller. Therefore, it is crucial to include the GPAs and power supply stages in the gradient system model to obtain an accurate nonlinear model that compensates for the droop.

Gradient chain characterization techniques such as the gradient impulse response function (GIRF)<sup>14–19</sup> or gradient modulation transfer function (GMTF)<sup>20,21</sup> are also based on the assumption that the gradient system behaves as a linear time-invariant system. The information acquired from these techniques is used for trajectory correction in the image reconstruction procedure. Ideally, the gradient waveforms are controlled precisely such that trajectory correction is unnecessary.

This study is an extended version of a previously presented conference abstract on gradient current waveform droop compensation.<sup>22</sup> Here, a nonlinear second-order

model that includes the GPA and power supply is introduced for the gradient chain. The focus of this work is the investigation of nonlinearities associated with the GPA and compensation for the imperfections of the GPA rather than those of the gradient coil. The state space averaging (SSA) method has been used in the literature<sup>23–27</sup> to model DC–DC power convertors in a steady state linearized around an operating point. We use the modified SSA method to characterize the switching GPAs, both steady-state and transient behavior, by considering nonlinear equations. The accuracy of the SSA method primarily depends on the switching frequency of pulse width modulation (PWM) signals. In our case, this method is applicable because of high-switching PWM signals (1 MHz). The digital inversion of the acquired model is then used in the feedforward open-loop configuration to provide the required voltage to control the output gradient currents. Using a nonlinear controller compensates for the current droop in the plateau region of the trapezoidal gradient waveforms and provides slight corrections in the transients. As proof of concept, this study considers a *z*-gradient coil with two separate windings driven by two independent GPAs and power supplies. A nonlinear multi-input-multi-output feedforward controller is applied. The output currents are measured for both linear and nonlinear controllers by applying a trapezoidal waveform at the input. Finally, MRI experiments are conducted to show the effectiveness of the proposed method.

## 2 | METHODS

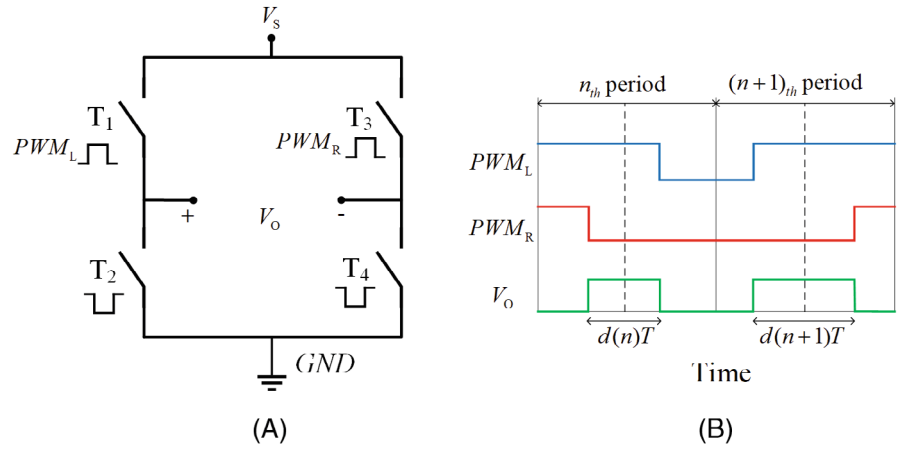
### 2.1 | Gradient power amplifier and PWM generation

Switch-mode full-bridge GPAs<sup>28,29</sup> are standard amplifier types used to drive MRI gradient coils with high current levels of several hundred amperes. These amplifiers operate by rapidly switching back and forth between the supply rails, which are being fed by PWM signals. In PWM, the frequency of pulses remains fixed, but the duration of each pulse is modulated according to the corresponding duty cycle. The duty cycle is calculated by dividing the required voltage by the power supply voltage (either a feedforward or feedback controller).

$$d = \frac{V_{\text{required}}}{V_S} \quad (1)$$

Note that *d* must be in the range of  $-1$  to  $1$ . The full-bridge amplifier configuration and center-aligned approach for PWM generation are shown in Figure 1A and B, respectively.

**FIGURE 1** A, Full-bridge power amplifier configuration. B, The center-aligned approach for two periods of PWM. The waveforms for the high-side transistors ( $T_1$  and  $T_3$ ) are shown in the figure. The low-side transistors ( $T_2$  and  $T_4$ ) are switched with complementary logic



Considering a feedforward configuration and for a given desired current waveform,  $i(t)$ , the required voltage can be calculated by the following equation:

$$v_{\text{required}}(t) = L \frac{di(t)}{dt} + Ri(t) \quad (2)$$

where  $L$  and  $R$  represent the inductance and resistance of the gradient coil, respectively. This linear equation can be extended for the gradient array<sup>3</sup> or multi-coil systems, in which case, the mutual inductance between the coils should be considered.

Equation (1) holds true if the drain voltages of the GPA metal-oxide semiconductor field effect transistors (MOSFETs) are constant and equal to the supply voltage, which yields a first-order linear model for the gradient systems. In practice, however, the supply voltage is not constant.

## 2.2 | Modified SSA

The SSA technique was developed to characterize switching power converters.<sup>24</sup> DC-DC power conversion is accomplished by repetitively switching between linear circuits with lossless storage components, inductances, and capacitances. Assuming a single period of PWM, there are only two different states of the circuit, that is, “on” and “off” (Figure 2). During the intervals  $T_{\text{on}}(nT < t < t_s)$  and  $T_{\text{off}}(t_s < t < (n+1)T)$ ,  $t_s$  is the switching time, and the following linear time-invariant differential equations can describe the system:

$$\frac{d\mathbf{x}(t)}{dt} = \begin{cases} \mathbf{A}_{\text{on}}\mathbf{x}(t) + \mathbf{b}_{\text{on}} & nT < t < t_s \\ \mathbf{A}_{\text{off}}\mathbf{x}(t) + \mathbf{b}_{\text{off}} & t_s < t < (n+1)T \end{cases} \quad (3)$$

This equation is the state-space representation of the differential equations, where  $\mathbf{x}$  is the state vector, which is composed of the inductor’s current and capacitor’s

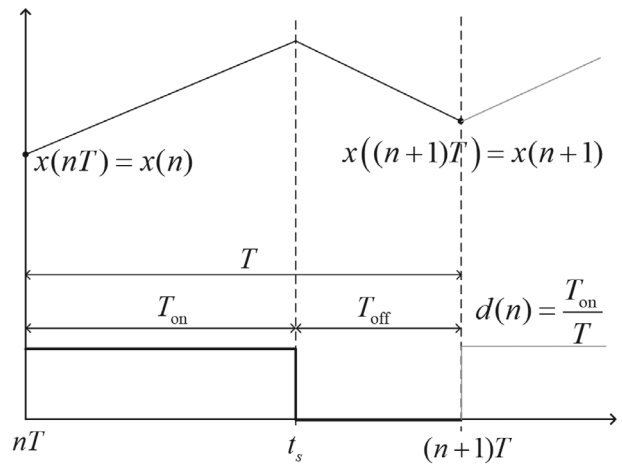


**FIGURE 2** A single circuit variable (the inductor current, for example) time dependence over a period of PWM ( $T$ ) with the PWM on and off duration. The duty cycle,  $d(n)$ , is defined as the ratio of  $T_{\text{on}}$  to  $T$

voltage. The state matrix  $\mathbf{A}_{\text{on}}$  and the input vector  $\mathbf{b}_{\text{on}}$  describe the circuit topology when it is in the “on” state. Likewise,  $\mathbf{A}_{\text{off}}$  and  $\mathbf{b}_{\text{off}}$  represent the “off” state. The corresponding solutions of the above equations are as follows:

$$\mathbf{x}(t) = \begin{cases} e^{\mathbf{A}_{\text{on}}(t-nT)}\mathbf{x}(nT) + \mathbf{A}_{\text{on}}^{-1}(e^{\mathbf{A}_{\text{on}}(t-nT)} - \mathbf{I})\mathbf{b}_{\text{on}} & nT < t < t_s \\ e^{\mathbf{A}_{\text{off}}(t-t_s)}\mathbf{x}(t_s) + \mathbf{A}_{\text{off}}^{-1}(e^{\mathbf{A}_{\text{off}}(t-t_s)} - \mathbf{I})\mathbf{b}_{\text{off}} & t_s < t < (n+1)T \end{cases} \quad (4)$$

Knowing that,  $t_s - nT = T_{\text{on}} = d(n)T$  and  $(n+1)T - t_s = T_{\text{off}} = (1 - d(n))T$ , at  $t = (n+1)T$ , we have the following:

$$\begin{aligned} \mathbf{x}((n+1)T) &= e^{\mathbf{A}_{\text{off}}(1-d(n))T} [e^{\mathbf{A}_{\text{on}}d(n)T}\mathbf{x}(nT) + \mathbf{A}_{\text{on}}^{-1}(e^{\mathbf{A}_{\text{on}}d(n)T} - \mathbf{I})\mathbf{b}_{\text{on}}] \\ &\quad + \mathbf{A}_{\text{off}}^{-1}(e^{\mathbf{A}_{\text{off}}(1-d(n))T} - \mathbf{I})\mathbf{b}_{\text{off}} \end{aligned} \quad (5)$$

Now, we use the first-order approximation of the fundamental matrix  $e^{At} \approx \mathbf{I} + \mathbf{A}t$  and keep only the first-order terms. By defining  $\mathbf{x}(n) = \mathbf{x}(nT)$ , the following difference equation describes the general behavior of the circuit:

$$\mathbf{x}(n+1) = \underbrace{\left[ \mathbf{I} + d(n)T\mathbf{A}_{\text{on}} + (1-d(n))T\mathbf{A}_{\text{off}} \right]}_{\mathbf{A}_{\text{avg}}} \mathbf{x}(n) + \underbrace{\left[ d(n)T\mathbf{b}_{\text{on}} + (1-d(n))T\mathbf{b}_{\text{off}} \right]}_{\mathbf{b}_{\text{avg}}} \quad (6)$$

where  $T$  is the sampling period,  $\mathbf{I}$  is the identity matrix, and  $d(n)$  is the duty cycle of period  $n_{th}$ , which is the main input of the system in DC-DC power converters.  $\mathbf{x}(n)$  and  $\mathbf{x}(n+1)$  are the state vectors at the beginning and the end of period  $n_{th}$ , respectively. The edge-aligned configuration is considered here for simplicity. However, it can be shown that the result is not a function of the phase; thus, the center-aligned PWM can be approximated with the same equation. Equation (6) describes the averaged behavior of the circuit, effectively smoothing out the switching ripple, and we call it the averaged model. In a linear system, the state matrix is a constant, and the input appears only in the additive term  $\mathbf{b}$ . However, the state matrix in Equation (6) ( $\mathbf{A}_{\text{avg}}$ ) incorporates the duty cycle, which is the input, making the system nonlinear, i.e., doubling the input does not simply double the output.

### 2.3 | Single-channel gradient system

The gradient system considered here includes the gradient coil, gradient power amplifier, power supply stage, and PWM generation block. The gradient system's input is the duty cycle, and the output is the gradient coil current  $i_{GC}$ . Since the switching frequency of our GPA is sufficiently high, the modified SSA technique introduced in the previous section is used to characterize the general behavior of the gradient system. Considering a single period of PWMs, the on and off states of the circuit, which are indicated by the green and red paths in Figure 3A, respectively, can be described with the following equations:

$$\frac{d}{dt} \begin{bmatrix} i_{GC}(t) \\ v_C(t) \end{bmatrix} = \begin{cases} \begin{bmatrix} -\frac{R_{GC}}{L_{GC}} & \frac{1}{L_{GC}} \\ -\frac{1}{C} & -\frac{1}{R_S C} \end{bmatrix} \begin{bmatrix} i_{GC}(t) \\ v_C(t) \end{bmatrix} + \begin{bmatrix} 0 \\ \frac{V_S}{R_S C} \end{bmatrix}, & \text{for interval } T_{\text{on}} \\ \begin{bmatrix} -\frac{R_{GC}}{L_{GC}} & 0 \\ 0 & -\frac{1}{R_S C} \end{bmatrix} \begin{bmatrix} i_{GC}(t) \\ v_C(t) \end{bmatrix} + \begin{bmatrix} 0 \\ \frac{V_S}{R_S C} \end{bmatrix}, & \text{for interval } T_{\text{off}} \end{cases} \quad (7)$$

The state variables are the gradient coil current and the decoupling capacitor voltage. The averaged nonlinear model can be formulated as follows:

$$\begin{bmatrix} i_{GC}(n+1) \\ v_C(n+1) \end{bmatrix} = \begin{bmatrix} 1 - \frac{TR_{GC}}{L_{GC}} & \frac{T}{L_{GC}}d(n) \\ -\frac{T}{C}d(n) & 1 - \frac{T}{R_S C} \end{bmatrix} \begin{bmatrix} i_{GC}(n) \\ v_C(n) \end{bmatrix} + \begin{bmatrix} 0 \\ \frac{TV_S}{R_S C} \end{bmatrix} \quad (8)$$

This equation shows the interdependency of the gradient current and capacitor voltage. If  $d$  is zero, at the steady state, the gradient coil current,  $i_{GC}$ , is zero. The capacitor voltage,  $v_C$ , becomes equal to the supply voltage,  $V_S$ . When  $d$  increases,  $v_C$  starts to decrease. As a result, the gradient current cannot follow the value of  $d$  and gradually decreases. This event is called droop in power electronics. The amount of droop depends on the circuit parameters and the magnitude of the current flowing in the coil. As the gradient coil current increases, the droop increases nonlinearly. It is worth mentioning that if we consider only the gradient coil model (ignoring the capacitor and power supply nonideality), the resulting equation will be the first-order linear equation used in previous works.<sup>3,30</sup>

### 2.4 | Multi-coil gradient system

The modified SSA technique can also be used to characterize gradient systems with coupled coils. As a proof of concept, we write equations for only a two-channel gradient; however, the technique can be easily generalized for a high number of channels. Assuming  $d_1 > d_2$  ( $d_1$ : channel 1 duty cycle,  $d_2$ : channel 2 duty cycle), there are only three different circuit states. During the intervals  $T_{\text{on-on}}$ ,  $T_{\text{on-off}}$ ,  $T_{\text{off-off}}$  (Figure 3B), the system can be described by a set of linear, time-invariant differential equations, as follows:

$$\frac{d\mathbf{x}(t)}{dt} = \begin{cases} \mathbf{A}_{\text{on-on}}\mathbf{x}(t) + \mathbf{b}_{\text{on-on}}, & \text{for interval } T_{\text{on-on}} \\ \mathbf{A}_{\text{on-off}}\mathbf{x}(t) + \mathbf{b}_{\text{on-off}}, & \text{for interval } T_{\text{on-off}} \\ \mathbf{A}_{\text{off-off}}\mathbf{x}(t) + \mathbf{b}_{\text{off-off}}, & \text{for interval } T_{\text{off-off}} \end{cases} \quad (9)$$

Similar to the single channel, under the rapid switching assumption, the circuit's general behavior can be described by a single difference equation, as follows:

$$\mathbf{x}(n+1) = \mathbf{A}(d_1(n), d_2(n))\mathbf{x}(n) + \mathbf{b}(d_1(n), d_2(n)) \quad (10)$$

where  $\mathbf{x}$  is the state vector consisting of the gradient coil current and capacitor voltage. Matrices  $\mathbf{A}$  and  $\mathbf{b}$  are ( $K$  is the mutual inductance between the coils and  $K = L_{GC1}L_{GC2} - M^2$ ) as follows:

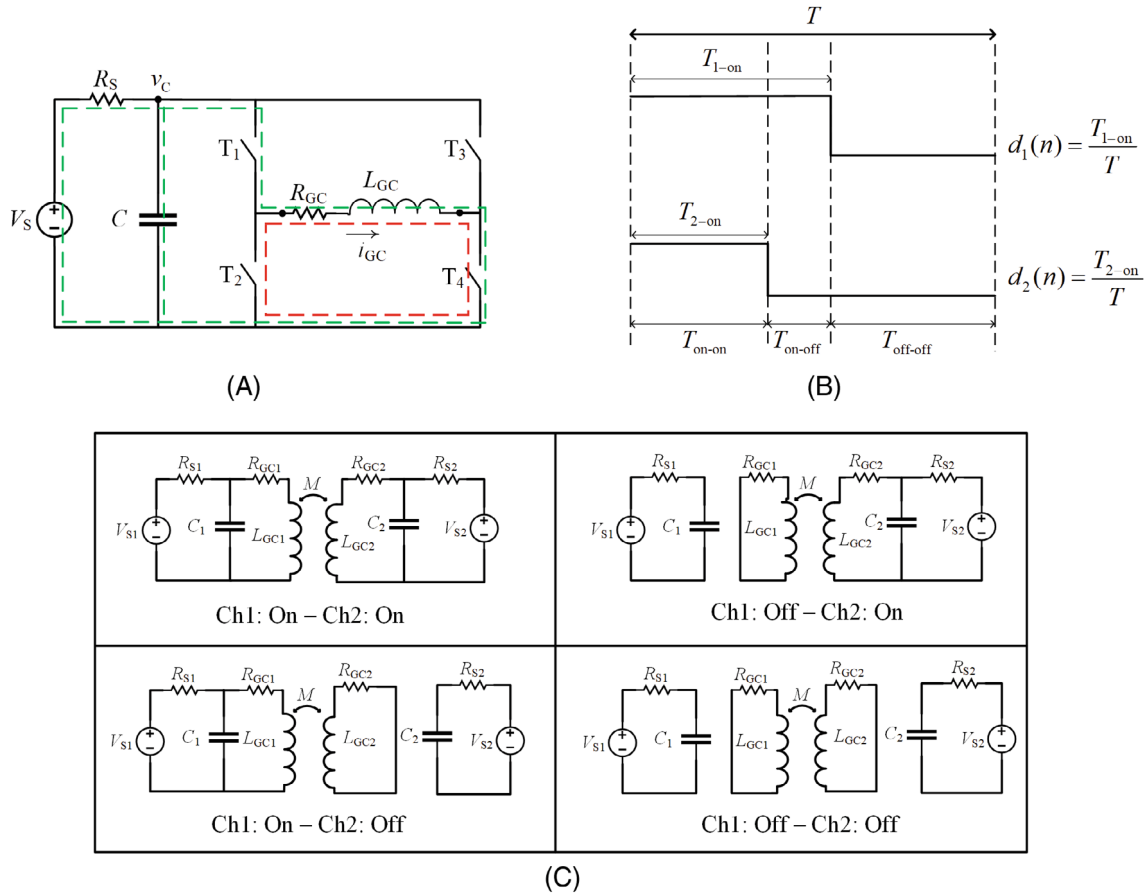


**FIGURE 3** A, Single-channel gradient system circuit including amplifier, power supply with parallel decoupling capacitor, and the gradient coil. The green path shows the circuit during  $T_{on}$ , and the red path shows the circuit during  $T_{off}$ . PWMs for channel 1 and channel 2 assuming  $d_1 > d_2$  (B) and different states of the two-channel system circuit that covers any combination of  $d_1, d_2$  (C)

$$\mathbf{A}(n) = \begin{bmatrix} 1 - \frac{TR_{GC1}L_{GC2}}{K} & \frac{TL_{GC2}}{K} d_1(n) & \frac{TM_{RGC2}}{K} & -\frac{TM}{K} d_2(n) \\ -\frac{T}{C_1} d_1(n) & 1 - \frac{T}{R_{S1}C_1} & 0 & 0 \\ \frac{TM_{RGC1}}{K} & -\frac{TM}{K} d_1(n) & 1 - \frac{TR_{GC2}L_1}{K} & \frac{TL_{GC1}}{K} d_2(n) \\ 0 & 0 & -\frac{T}{C_2} d_2(n) & 1 - \frac{T}{R_{S2}C_2} \end{bmatrix},$$

$$\mathbf{b} = \begin{bmatrix} 0 & 0 \\ \frac{TV_{S1}}{R_{S1}C_1} & 0 \\ 0 & 0 \\ 0 & \frac{TV_{S2}}{R_{S2}C_2} \end{bmatrix} \quad (11)$$

### 2.5 | Control architecture

The performance of the gradient system greatly depends on the selected control method. The feedback control (proportional-integral-derivative) method has been widely used to regulate the gradient current waveforms; however, this method limits bandwidth of the gradient system and necessitates high-precision current sensors, raising the system's cost. In contrast, feedforward

controllers do not need current measurements and have higher bandwidth but require an accurate system model. Although a linear model consisting of only gradient coil parameters (inductance and resistance) may provide a good approximation of the system, it does not cover the nonlinear behavior of GPAs and power supply stages. Therefore, improved characterization of the gradient system, which includes those nonlinearities, is essential.

To find the feedforward controller, we use the inverse of the proposed averaged nonlinear model. The duty cycle is extracted from the desired gradient current waveform and the calculated capacitor voltage in the discrete-time domain. As an example, for a single-channel gradient system, the following two recursive equations represent the inverse system (feedforward controller):

$$d(n) = \frac{\frac{L_{GC}}{T} (i_{dGC}(n+1) - i_{dGC}(n)) + R_{GC} i_{dGC}(n)}{v_C(n)} \quad (12)$$

$$v_C(n+1) = \left(1 - \frac{T}{R_S C}\right) v_C(n) - \frac{T}{C} d(n) i_{dGC}(n) + \frac{TV_S}{R_S C} \quad (13)$$

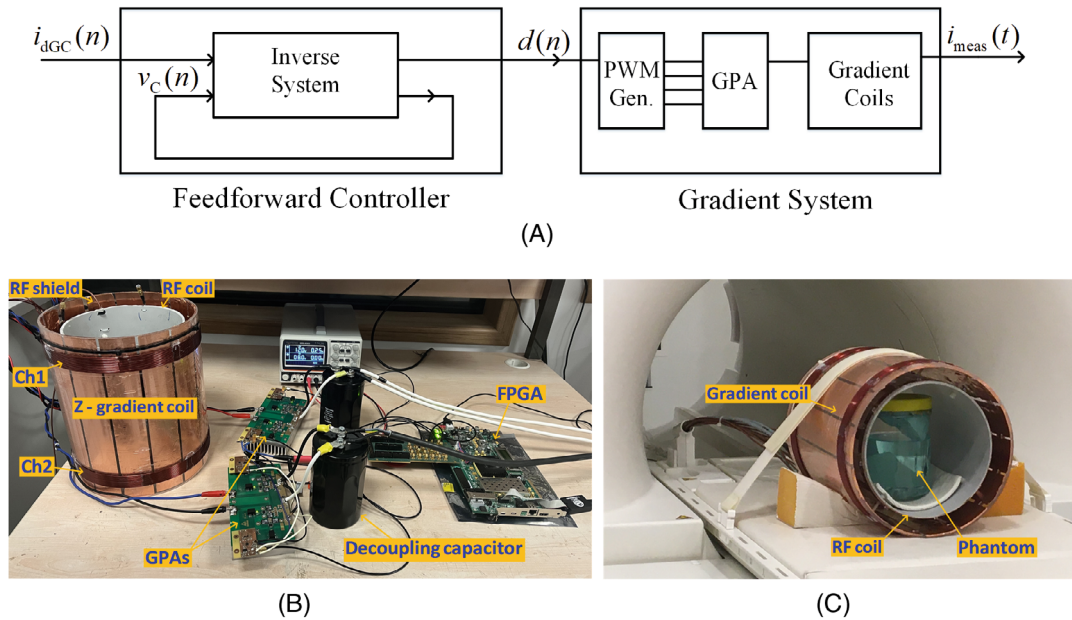


**FIGURE 4** A, The overall gradient chain block diagram, including the feedforward controller and different components of the gradient system. B, Benchtop installation, which is located in the equipment room. C, The imaging setup, including the gradient coil, RF coil, TR switch, and phantom

where  $d(n)$  is the duty cycle of the  $n_{th}$  PWM and,  $i_{dGC}(n)$  and  $v_C(n)$  are the desired gradient current waveform and the calculated capacitor voltage, respectively. Since the desired current is known at all-time points and the initial capacitor voltage is the supply voltage,  $d(n)$  can be computed using Equation (12). The following values of  $v_C(n)$  will be calculated using Equation (13). The output of the feedforward controller is the duty cycle, which is used to generate the PWM signals. These equations can be easily extended to a high number of channels. Figure 4A depicts the block diagram of the feedforward controller (inverse system) and the gradient system itself.

The Xilinx Virtex-VC707 evaluation board is used for the digital implementation of the feedforward controller (Equations 12 and 13) and PWM signal generation. A center-aligned PWM with a 500 kHz switching frequency (1 MHz effective frequency at the output, which leads to a 1  $\mu$ s dwell time) is used to drive the GPA switches. The computation of the feedforward controller and PWM generation is fast enough to be completed in a dwell time, making it a real-time process. The computational speed depends on the field-programmable gate array resources and the clock frequency used for calculations. In our case, the lookup table use is 4503 out of 303,600 (1.48%) for a single channel. The pipelined architecture is used to maximize the clock frequency. The resource use increases as the number of channels increases, but not linearly due to mutual couplings between channels. For a high number of channels, the field-programmable gate array resources may not be sufficient to compute all channels in parallel

within a dwell time, resulting in a computational delay. However, the real-time operation will not be compromised because a known fixed delay in an open-loop configuration can be easily handled by injecting the input signal in advance.

The resolution of PWMs has a significant impact on the nonlinear feedforward controller's efficiency. High-resolution PWMs must be sensitive enough to detect small changes in the applied duty cycle. For this purpose, a 400 MHz clock frequency is used as the main counter, resulting in a 10-bit resolution. An additional 5 bits are added by using field-programmable gate array delay elements to achieve a 15-bit time resolution (78 ps), which significantly reduces the digitization error in the gradient waveforms.<sup>31</sup>

## 2.6 | SSA model and feedforward control simulations

To demonstrate how accurately the SSA model follows the topological model, the responses of both models to two different inputs (constant and varying duty cycles) are compared in the simulation. The topological model is the exact circuit implementation, including the switching function (the circuit shown in Figure 3A). Gradient coil current simulations are also carried out using linear and nonlinear controllers with a trapezoidal waveform as the input to illustrate the capability of the nonlinear controller in droop compensation. Because the image quality

directly depends on the integral of the gradient (current) waveform, the time integral of the desired test waveform is compared to the time integrals of waveforms generated using the linear and nonlinear controllers. MATLAB (R2020b, The MathWorks, Natick, MA) is used to conduct all simulations.

## 2.7 | Hardware setup

Custom-built fast switching power amplifiers consist of new generation enhancement mode gallium nitride (eGaN) power transistors, which can operate reliability under high-voltage, high-temperature, and high-frequency, are used to provide the required voltage level to the gradient coil using the appropriate duty cycle. The fabricated GPAs are designed to be capable of 400 V/100 A operation ratings; however, smaller ratings were tested to prudent. It is worth mentioning that our GPA costs less than \$200, which is comparable to the existing low-cost gradient amplifiers,<sup>32,33</sup> but operates at higher power levels. The switching frequency in a conventional GPA is approximately 100 kHz; however, by using eGaN transistors,<sup>34</sup> it is possible to increase the switching frequency to 500 kHz, which results in a reduction of current ripples without LC low-pass filters or other ripple attenuation techniques.<sup>35–37</sup> The dead time adjustments made to avoid shoot-through currents are performed by resistor-capacitor circuits on the GPAs board. The transistor temperature is monitored using a thermal camera to ensure that the high switching frequency does not reduce the efficiency of the GPA.

A two-channel *z*-gradient coil is used as a Maxwell pair, producing a linear gradient field inside the region of interest. Each coil is made up of 12 turns wound on cylindrical Plexiglas with a diameter of 25 cm. Both coils have almost the same inductance and resistance, which are 80  $\mu$ H and 200 m $\Omega$ , respectively. The mutual inductance between the coils is approximately 25  $\mu$ H. The large bulk capacitors (5600  $\mu$ F) connected to the power supply ( $V_S$ ) work to decouple the GPAs from the power supplies and provide the majority of the switching current required by the amplifier. The resistance between the power supplies and GPAs was calculated by dividing the measured voltage difference by the current. These parameters are tuned to take into account the effect of cables and switches on-resistance ( $R_{ds-on}$ ).

## 2.8 | Gradient current measurements

As a proof of concept, two different trapezoids (one with a 50 A amplitude and the other with a 10 A

amplitude) are applied as inputs to the first and second channels of the *z*-gradient coil. For both channels, the rise time and pulse duration are 200  $\mu$ s and 8 ms, respectively. Each channel is driven by an independent amplifier and power supply (Agilent-N8740A, 150 V maximum voltage). The currents are measured using an Agilent-1146B AC/DC current probe on the lab bench (Figure 4B).

Current measurements are also performed before imaging by placing the gradient coil into the scanner bore. Upon switching the gradient coil on/off, decaying oscillations are observed on the gradient current. While the exact mechanism is not well understood, the mechanical vibration<sup>38,39</sup> caused by Lorentz forces and/or gradient-induced eddy currents<sup>40</sup> could be the possible sources of this oscillatory behavior. Because nonlinearities in the system have already been corrected, linear time-invariant system theory and, thus, the gradient current transfer function can be used to compensate for these oscillations. The measured output current (with oscillations) is divided by the desired input in the frequency domain to obtain the current transfer function. Using this transfer function yields a premodified input that produces the desired trapezoid at the output.

## 2.9 | MRI experiments

MRI experiments are conducted on a Siemens TimTrio 3 T scanner. The imaging setup includes gradient coils that are connected to the GPAs (outside the scanner room) via a feedthrough panel. Trapezoidal waveforms are used to drive both coils with opposite polarity to generate a linear gradient field. We use a home-built, homogeneous cylindrical phantom (diameter of 10 cm) that consists of a CuSO<sub>4</sub> solution at a concentration of 15 mM/L. A single coronal slice (*X-Z* plane) is imaged using a gradient echo sequence (with a slice thickness of 5 mm and a field of view of 250 mm). During the experiments, the scanner *z*-gradient is inactivated, and the provided *z*-gradient coil is used to generate the required dephasing and readout gradients with a strength of 6.2 mT/m in the *z*-direction. The total durations of the dephasing and readout gradients are 2250  $\mu$ s and 4500  $\mu$ s, respectively, including rise/fall times of 220  $\mu$ s. The TE/TR values are 10/20 ms. The slice selection and phase encoding gradients are applied via the scanner. A trigger signal is taken from the scanner to synchronize the timings between system gradients and our applied gradient. For RF transmission and reception, a home-built shielded Tx/Rx birdcage coil is placed inside the gradient coil. Figure 4C shows the imaging setup.

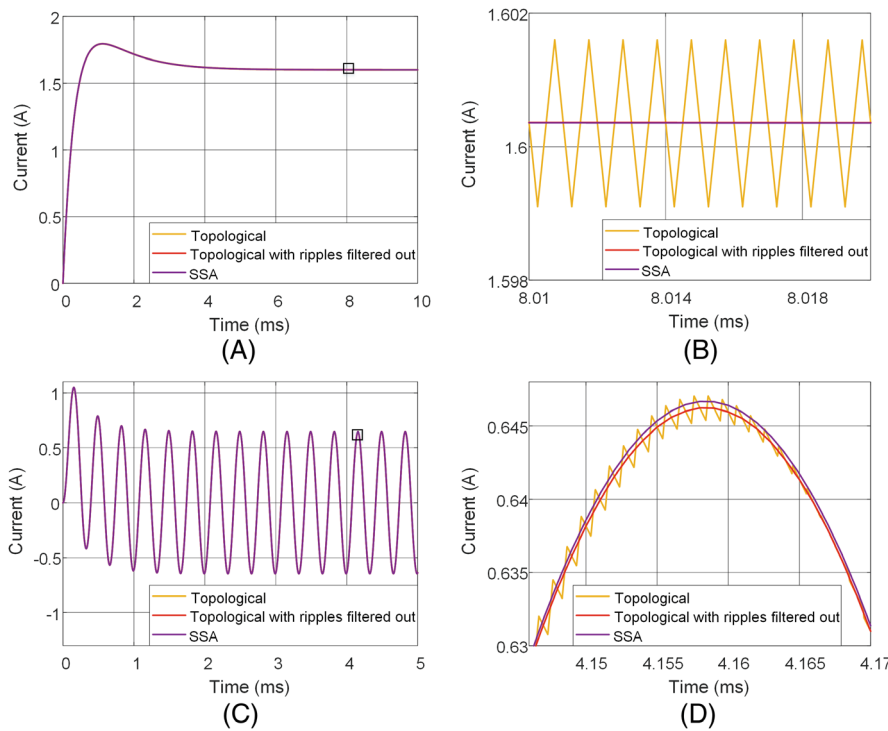


**FIGURE 5** Time response comparison of the topological model of the gradient system (yellow) and the SSA model (purple). The red curve shows the average of the topological model with ripples filtered out. A, Constant duty cycle,  $d = 0.5$ . B, Magnified view of a small region depicted by a square in Panel A. The topological model average is precisely followed by the SSA model (normalized maximum error =  $3.4 \times 10^{-4}\%$ ). Varying duty cycle (3 kHz sinusoidal) (C), and magnified view of the region specified by the square in Panel C (D). Even in this case, i.e., varying duty cycle, the SSA provides an excellent approximation of the topological model (normalized maximum error = 0.11%). This error is duty cycle-dependent, and it increases as the duty cycle increases. A frequency of 3 kHz (as an example) is used here, which is within the common range of the gradient operation frequency

### 3 | RESULTS

#### 3.1 | State-space averaging method

Figure 5 depicts the responses of SSA (Equation 8) and topological models to a constant duty cycle (Figure 5A) and a varying duty cycle (3 kHz sinusoidal waveform, Figure 5C) for a single-channel gradient system, validating the accuracy of the SSA method in approximating the circuit behavior. The normalized maximum error between the SSA model and the average of the topological model (ripples filtered out) for the constant and varying duty cycles are  $3.4 \times 10^{-4}\%$  and 0.11%, respectively. This error is duty cycle-dependent, and it increases as the duty cycle increases, as shown in Figure 5D. The current ripples (at the switching frequency) are visible in the topological model response (Figure 5B) due to the GPA switching behavior. Because of the lack of switching frequency parameters in the SSA model, it cannot simulate ripples.

#### 3.2 | Feedforward control simulations

Figure 6 compares the performance of the proposed nonlinear controller to that of the linear controller when a trapezoidal input is applied. The linear controller produces a constant duty cycle in the flat-top region; however, the nonlinear controller provides exponentially increasing duty cycles in that region to compensate for the droop. The maximum difference between these two occurs near

the end of the flat-top region, showing a 2.3% increase in the duty cycles. The output currents (gradient coil currents) generated by the linear and nonlinear controllers are shown in Figure 6C and D. Due to the limited resolution of PWM signals, some undesirable low-frequency oscillations (8 mA peak-to-peak amplitude) can be observed in the trapezoid plateau, as explained in the discussion. In the simulations, the integral error for the linear controller is approximately 1.4%, and it is almost zero (0.0014%) when the nonlinear controller is used.

#### 3.3 | Gradient current measurements

Figure 7 shows benchtop measurements of coil currents generated by linear and nonlinear controllers. Because there is no feedback loop to regulate the output currents, the current droop is visible in the flat-top region when using the linear controller; however, the nonlinear controller compensates for the droop. The gradient integral errors for the waveforms generated by linear and nonlinear controllers are 1.9% and 0.13%, respectively. The nonlinear controller outperforms the linear controller by reducing the integral error 14-fold, proving its droop compensation capability. Figure 8 depicts the gradient coil current generated by the nonlinear controller when the coil is placed inside the scanner bore, and as explained in Section 2.7, the oscillatory response can be observed on the current (red waveform) as the gradient turns on and off. Applying a premodified input current obtained through the current



**FIGURE 6** Simulation results. A, Calculated required duty cycles for linear first-order and nonlinear second-order models. B, A magnified view of the flat-top region, which clearly shows the difference between the outputs of linear and nonlinear controllers. C, The gradient coil's current after applying the duty cycles acquired in Panel A. This demonstrates that the nonlinear controller compensates for the current droop in the flat top region. D, A magnified view of C for the flat-top period

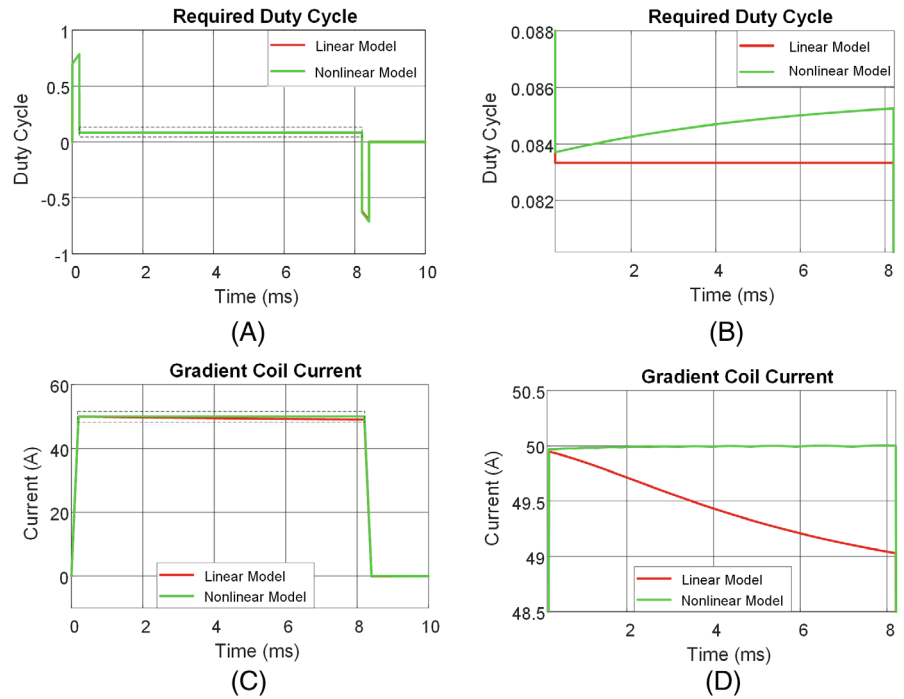
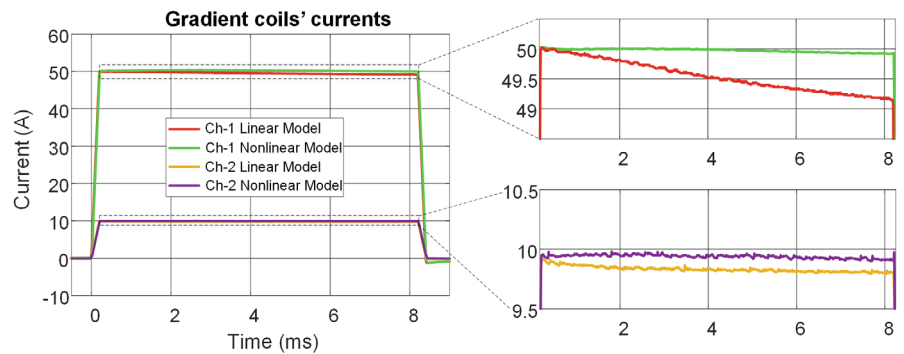


**FIGURE 7** Experimental results. Comparison of the coils' currents generated using the linear and nonlinear models. The reference inputs are trapezoid waveforms with amplitudes of 50 A and 10 A for channel 1 and channel 2, respectively. Both channels have the same rise time (200  $\mu$ s)



transfer function suppresses the oscillatory behavior and generates an oscillation-free trapezoid (green waveform).

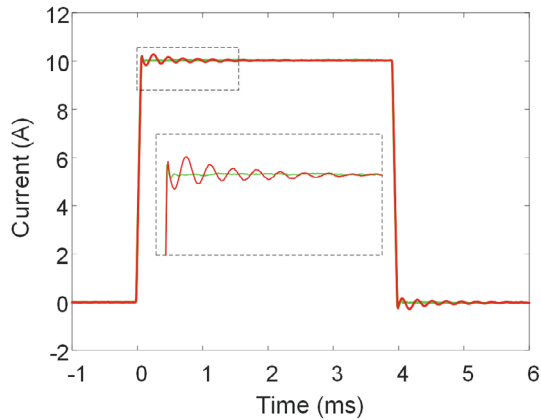
### 3.4 | MRI experiments

Figure 9 (first row) shows the phantom images acquired in the coronal plane. The reference image was obtained using the scanner gradients. The uncompensated/compensated image was taken with the home-built  $z$ -gradient coil that generates readout gradients using the linear/nonlinear controller. The droop in the readout gradient caused the gradient magnitude to deviate from its desired value, resulting in image deformation (shrinking) along the readout direction. The yellow arrows indicate these deformations. The nonlinear controller, which compensates for the droop and provides almost the desired gradient waveform, corrected these deformations. The difference images (uncompensated and compensated images were

subtracted from the reference image) are shown in the second row. The line profiles of the difference images show an error in the intensity of six pixels for the uncompensated image (red line), which is nearly corrected in the compensated image (green line). Although the intensity of the images taken with our gradient coil is higher than the reference image in some areas, the main goal is to compare the performances of linear and nonlinear controllers. These images validate the claim that, in a gradient system without feedback control, the gradient chain should be treated as a nonlinear system and a nonlinear feedforward controller should be used to eliminate imperfections in the GPA and power supply.

### 4 | DISCUSSION

In this study, a modified state-space averaging method was used to characterize the gradient system. The nonlinear



**FIGURE 8** Oscillations of the current after switching the gradient coil inside the scanner on/off (the red waveform). These oscillations are removed by using the gradient current transfer function and modifying the input waveform accordingly (the green waveform)

effects of switching gradient power amplifiers were formulated, and a method to compensate for the current droop was proposed. The SSA method has been used in the

literature<sup>25</sup> to model the transfer properties of power converters by linearizing the equations around an operating point; however, to find an accurate model for the gradient system, we considered nonlinear equations. The main assumption in this method is the approximation of the fundamental matrix by its first-order linear term, which is applicable in our case due to high-frequency PWMs. Using high-order terms will, of course, improve the modeling accuracy; however, the first-order term is preferred to avoid calculation complexity. In the circuit model, the amplifier switches (MOSFETs) are replaced by ideal switches and series resistances ( $R_{ds-on}$ ), the gradient coil is modeled as an inductance in series with a resistance, and the power supply stage is represented with only an ideal DC voltage source and an resistor-capacitor circuit. Considering the parasitic elements in the circuit model would result in a more accurate characterization. Therefore, the gradient system was modeled as a nonlinear, time-invariant system. The digital inverse of this model was used in the feedforward path (open loop) to control the PWM duty cycle and thus the output current.

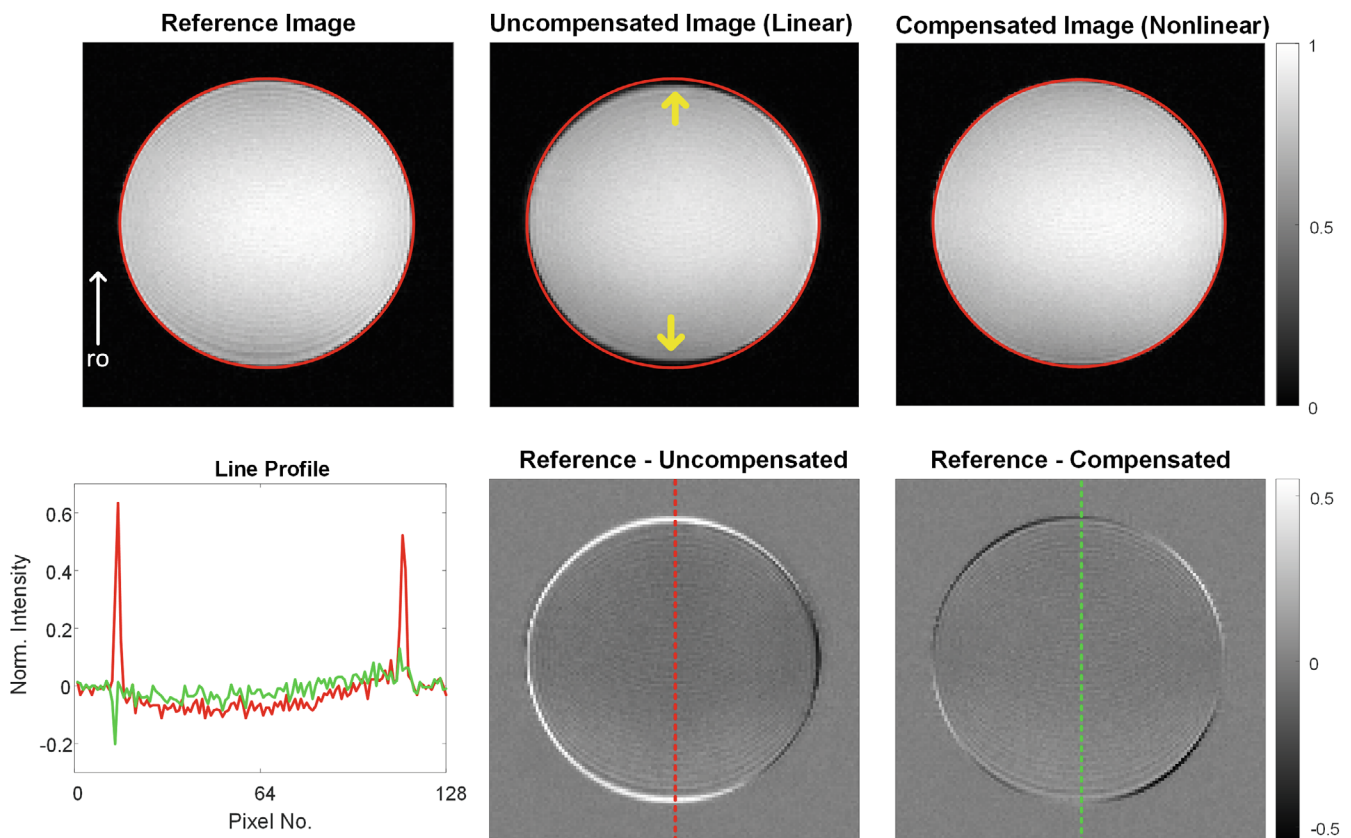


**FIGURE 9** Phantom images acquired in the coronal plane using the gradient echo pulse sequence (single slice). The uncompensated and compensated images are taken by applying the currents provided with the linear and nonlinear controllers, respectively, as a readout gradient (in the  $z$  direction, indicated by the white arrow). The droop in the readout gradient when using the linear controller results in image deformation (shrinking), which is indicated by yellow arrows. The normalized error images and the line profiles show a significant improvement in the image quality for the compensated image (acquired using the nonlinear controller)

The gradient system model and, consequently, the feedforward controller (both linear and nonlinear models) are susceptible to the circuit parameters. The circuit model lumped elements are assumed to be constant in the operating bandwidth, but resistances may change due to temperature variation and affect the output gradient current. The feedforward controller is also prone to external disturbances such as eddy currents and mechanical vibrations. These issues are related to the gradient coil, but the focus of this work is on the investigation of nonlinearities associated with the GPA. Although the resistances of the GPA switches ( $R_{ds-on}$ ) are also temperature-dependent, the coil resistance (including connection cables) is dominant, so the GPA thermal effects on the output current are negligible.

We used low duty cycle (5%) pulses in measurements to distinguish the GPA nonlinearity from the coil thermal effects. The thermal effects due to temperature-dependent resistances are mostly related to the gradient coil and not the amplifier; therefore, for high-duty cycle applications, an assessment of the gradient coil thermal behavior is necessary. The coil thermal behavior can also be characterized, and the temperature-dependent parameters of the feedforward controller can be adaptively updated based on the thermal model.

Although a closed-loop feedback (proportional-integral-derivative) controller<sup>1</sup> can achieve similar results on its own, it requires high-precision current sensors, which significantly raises the system cost for array<sup>3</sup> or multi-coil<sup>6</sup> systems with increased channels. The performances of feedback and feedforward controllers can also be compared, which is left for future investigations. The combination of feedforward and feedback controllers<sup>41</sup> can also be used to eliminate residual errors caused by time-varying (temperature-dependent) parameters, eddy currents, and mechanical vibrations; in this case, the nonlinear feedforward controller markedly reduces the load of the feedback loop.

High-resolution PWM signals<sup>31</sup> are essential to ensure proper functionality of the nonlinear controller. In some regions (e.g., the trapezoid plateau), the difference in the duty cycle of consecutive PWMs is small, and if the PWM generation algorithm does not provide enough resolution to detect those slight variations, a series of PWMs will have the same duty cycle, resulting in an unwanted low-frequency oscillation at the output current. Here, the PWM duty cycles are generated with 15 bits, corresponding to a temporal resolution of less than 80 ps, minimizing those oscillations. The oscillations mentioned above are distinct from the current ripples caused by the switching nature of amplifiers.<sup>35</sup>

One of the benefits of high-frequency switching PWMs is the reduction of output current ripples. As the

switching frequency increases, the current ripples become small enough that LC filter stages at the GPA output are no longer required, resulting in additional cost savings. In the case of using ripple cancelation filters, the gradient system characterization should also take into account the filter circuit model. Another potential advantage is the broadening of the operational bandwidth, even in closed-loop controllers. As a result of the shorter dwell time, gradient waveforms with higher slew rates (lower rise time) can be generated.

The nonlinear feedforward controller is also applicable for varying loads. Because the feedforward controller depends on the system model (circuit parameters), any changes in the parameters must be reflected in the feedforward controller. For example, in the case of driving a group of coil elements with a single amplifier by means of switching circuits,<sup>42</sup> the coil-related parameters of the controller must be updated. This is easily accomplished by storing all coil parameters in the field-programmable gate array memory and loading the corresponding one when switching between coil elements occurs.

In the recently introduced array coil or multi-coil techniques, gradient coils have lower inductances than conventional coils; thus, it is possible to achieve the required current waveforms (with the desired amplitude and slew rate) by applying lower voltages. As the voltage/current ratio decreases, the current droop in the plateau region of the trapezoid waveform increases, and minor distortions appear in the rise/fall portions. Applying higher voltages (to achieve the same current) might minimize the droop effect, but it increases the needed power and hardware cost. The proposed method compensates for the droop by adjusting the PWM duty cycles while using the optimum supply voltages.

Sizeable high-voltage capacitors (decoupling capacitors) connected in parallel to the power supplies are primarily responsible for high switching voltages and currents (the rise/fall portions of the trapezoid). Since the maximum required voltage for the array coils is less than that of the conventional coils, smaller capacitors with lower voltages can be used. Although lowering the capacitor value may result in more droop, it does not affect the output current since the capacitor voltage droop is considered in the nonlinear model calculations. As a result, the proposed method allows for smaller capacitors, lowering system costs and physical space requirements without compromising the output quality.

In our experiments, the proposed method was only tested on the *z*-gradient and the readout gradient of a simple gradient echo sequence as a proof of concept; however, we expect similar results and performances for *x*- and *y*-gradients because the gradient chain circuit is the same for all three axes, and it can also be used to generate any

gradient waveform and compensate for the current droops. The effect of droop in the gradient current waveforms can be more pronounced in other applications, such as EPI and DWI, which require long pulses or high gradient strength, resulting in signal drop and image artifacts.

## 5 | CONCLUSIONS

This work presented and validated a modified state-space averaging technique for characterizing gradient system (including GPA and power supply), as well as a nonlinear feedforward controller for compensating for gradient current droop. The simulation results demonstrated that the SSA method provided an accurate gradient system characterization. The experimental results showed that using the nonlinear controller reduces the gradient current integral error 14-fold when compared to the linear controller. Phantom images verify the nonlinear controller performance in correcting distortions caused by gradient current droop.


## ACKNOWLEDGMENTS

ASELSAN provided the gradient power amplifiers. The authors would like to thank Volkan Acikel and Soheil Taraghinia for their assistance with the amplifier functionality.

## DATA AVAILABILITY STATEMENT

MATLAB and VHDL codes that reproduce the results are available openly at [https://github.com/UMRAM-Bilkent/Gradient\\_Feedforward](https://github.com/UMRAM-Bilkent/Gradient_Feedforward).

## ORCID

Reza Babaloo  <https://orcid.org/0000-0002-2604-6491>

Ergin Atalar  <https://orcid.org/0000-0002-6874-6103>

## REFERENCES

- Kimmlingen R, Gebhardt M, Schuster J, Brand M, Schmitt F, Haase A. Gradient system providing continuously variable field characteristics. *Magn Reson Med*. 2002;47:800-808.
- Lenz H, inventor; Siemens AG, assignee. Gradient amplifier with combined current regulation and differential control. US patent 6,448,775. September 10, 2002.
- Ertan K, Taraghinia S, Atalar E. Driving mutually coupled gradient array coils in magnetic resonance imaging. *Magn Reson Med*. 2019;82:1187-1198.
- Ertan K, Taraghinia S, Sadeghi A, Atalar E. A z-gradient array for simultaneous multi-slice excitation with a single-band RF pulse. *Magn Reson Med*. 2018;80:400-412.
- Ertan K, Taraghinia S, Saritas EU, Atalar E. Local optimization of diffusion encoding gradients using a z-gradient array for echo time reduction in DWI. In *Proceedings of the 26th Joint Annual Meeting of ISMRM-ESMRMB*, Paris, France, 2018. Abstract 1641.
- Juchem C, Nahhass OM, Nixon TW, de Graaf RA. Multi-slice MRI with the dynamic multi-coil technique. *NMR Biomed*. 2015;28:1526-1534.
- Juchem C, Nixon TW, McIntyre S, Rothman DL, de Graaf RA. Magnetic field modeling with a set of individual localized coils. *J Magn Reson*. 2010;204:281-289.
- Smith E, Freschi F, Repetto M, Crozier S. The coil array method for creating a dynamic imaging volume. *Magn Reson Med*. 2017;78:784-793.
- Jia F, Littin S, Layton KJ, Kroboth S, Yu H, Zaitsev M. Design of a shielded coil element of a matrix gradient coil. *J Magn Reson*. 2017;281:217-228.
- Littin S, Jia F, Layton KJ, et al. Development and implementation of an 84-channel matrix gradient coil. *Magn Reson Med*. 2018;79:1181-1191.
- Kundur P. *Power System Stability and Control*. The McGrath-Hill Companies; 1994.
- Lenz H, inventor; Siemens AG, assignee. Circuit arrangement, gradient amplifier, and method for compensating for nonlinearities of an amplifier output stage. US patent 9,897,673. February 20, 2018.
- Scheel T, Hattrup C, inventors; Koninklijke Philips NV, assignee. Gradient amplifier with compensation for dead time and forward voltage. US Patent 10,024,937. July 17, 2018.
- Campbell-Washburn AE, Xue H, Lederman RJ, Faranesh AZ, Hansen MS. Real-time distortion correction of spiral and echo planar images using the gradient system impulse response function. *Magn Reson Med*. 2016;75:2278-2285.
- Rahmer J, Mazurkewitz P, Börnert P, Nielsen T. Rapid acquisition of the 3D MRI gradient impulse response function using a simple phantom measurement. *Magn Reson Med*. 2019;82:2146-2159.
- Vannesjo SJ, Graedel NN, Kasper L, et al. Image reconstruction using a gradient impulse response model for trajectory prediction. *Magn Reson Med*. 2016;76:45-58.
- Vannesjo SJ, Haeberlin M, Kasper L, et al. Gradient system characterization by impulse response measurements with a dynamic field camera. *Magn Reson Med*. 2013;69:583-593.
- Vannesjo SJ, Duerst Y, Vionnet L, et al. Gradient and shim pre-emphasis by inversion of a linear time-invariant system model. *Magn Reson Med*. 2017;78:1607-1622.
- Kronthaler S, Rahmer J, Börnert P, et al. Trajectory correction based on the gradient impulse response function improves high-resolution UTE imaging of the musculoskeletal system. *Magn Reson Med*. 2021;85:2001-2015.
- Knopp T, Biederer S, Sattel TF, Erbe M, Buzug TM. Prediction of the spatial resolution of magnetic particle imaging using the modulation transfer function of the imaging process. *IEEE Trans Med Imaging*. 2011;30:1284-1292.
- Stich M, Wech T, Slawig A, et al. Gradient waveform pre-emphasis based on the gradient system transfer function. *Magn Reson Med*. 2018;80:1521-1532.
- Babaloo R, Taraghinia S, Atalar E. Droop compensation of gradient current waveforms in gradient array systems. In *Proceedings of the 29th Annual Meeting of ISMRM*, Virtual Exhibition, 2021. Abstract 3093.

23. Mahdavi J, Nasiri MR, Agah A, Emadi A. Application of neural networks and state-space averaging to DC/DC PWM converters in sliding-mode operation. *IEEE ASME Trans Mechatron.* 2005;10:60-67.
24. Middlebrook RD, Čuk S. A general unified approach to modelling switching-converter power stages. *Int J Electron Theor Exp.* 1977;42:521-550.
25. Ngamkong P, Kochcha P, Areerak K, Sujitjorn S, Areerak K. Applications of the generalized state-space averaging method to modelling of DC–DC power converters. *Math Comput Model Dyn Syst.* 2012;18:243-260.
26. Sanders SR, Noworolski JM, Liu XZ, Verghese GC. Generalized averaging method for power conversion circuits. *IEEE Trans Power Electron.* 1991;6:251-259.
27. Xu J, Lee C. Generalized state-space averaging approach for a class of periodically switched networks. *IEEE Tran Circuits Syst I: Fundam Theory Appl.* 1997;44:1078-1081.
28. Sabate J, Garces LJ, Szczesny PM, Li Q, Wirth WF. High-power high-fidelity switching amplifier driving gradient coils for MRI systems. *IEEE 35th Annual Power Electronics Specialists Conference, Aachen, Germany, 2004.* p. 261-266.
29. Sabate JA, Zhang RS, Garces LJ, Szczesny PM, Li Q, Wirth WF, inventors; General Electric Co, assignee. High fidelity, high power switched amplifier. US patent 7,116,166. October 3, 2006.
30. Sabate JA, Wang RR, Tao F, Chi S. Magnetic resonance imaging power: high-performance MVA gradient drivers. *IEEE J Emerg Sel Top Power Electron.* 2015;4:280-292.
31. Acikel V, Dogan A, Filci FE, Cansiz G, Atalar E. High resolution PWM generation for high frequency switching gradient amplifier control. In *Proceedings of the 27th Annual Meeting of ISMRM, Montréal, Québec, Canada, 2019.* Abstract 1600.
32. Cooley CZ, Stockmann JP, Witzel T, et al. Design and implementation of a low-cost, tabletop MRI scanner for education and research prototyping. *J Magn Reson.* 2020;310:106625.
33. Evetts N, Conradi MS. Low-cost gradient amplifiers for small MRI systems. *J Magn Reson.* 2022;335:107-127.
34. Taraghinia S, Acikel V, Babaloo R, Atalar E. Design and implementation of high switching frequency gradient power amplifier using eGaN devices. In *Proceedings of the 29th Annual Meeting of ISMRM, Virtual Exhibition, 2021.* Abstract 3092.
35. Sabate J, Schutten M, Steigerwald R, Li Q, Wirth WF. Ripple cancellation filter for magnetic resonance imaging gradient amplifiers. *19th Annual IEEE Applied Power Electronics Conference and Exposition; 2. IEEE; 2004:792-796.*
36. Taraghinia S, Ertan K, Atalar E. Minimum current ripple in the gradient array system by applying optimum-phase pulse-width modulation pattern. In *Proceedings of the 25th Annual Meeting of ISMRM, Honolulu, HI, 2017.* Abstract 2686.
37. Taraghinia S, Ertan K, Yardim A, Atalar E. Efficient ripple current reduction in gradient array system using optimized-phase control signals with one stage LC filter. In *Proceedings of the 34th Annual Meeting of ESMRMB, Barcelona, Spain, 2017.* Abstract 892.
38. Yao G, Mechefske C, Rutt B. Characterization of vibration and acoustic noise in a gradient-coil insert. *Magn Reson Mater Phys Biol Med.* 2004;17:12-27.
39. Nixon TW, McIntyre S, Rothman DL, de Graaf RA. Compensation of gradient-induced magnetic field perturbations. *J Magn Reson.* 2008;192:209-217.
40. Ryner L, Stroman P, Wessel T, Hoult D, Saunders J. Effect of oscillatory eddy currents on MR spectroscopy. In *Proceedings of the 6th Annual Meeting of the ISMRM, Sydney, NSW, Australia, 1998.* p. 1903.
41. Babaloo R, Taraghinia S, Acikel V, Takrimi M, Atalar E. Digital feedback design for mutual coupling compensation in gradient array system. In *Proceedings of the 28th Annual Meeting of ISMRM, Virtual Exhibition, 2020.* Abstract 4235.
42. Kroboth S, Layton KJ, Jia F, et al. Optimization of coil element configurations for a matrix gradient coil. *IEEE Trans Med Imaging.* 2017;37:284-292.

**How to cite this article:** Babaloo R, Atalar E. Nonlinear droop compensation for current waveforms in MRI gradient systems. *Magn Reson Med.* 2022;88:973-985. doi: 10.1002/mrm.29246